

Molecular Gas Density Measured with H₂CO and CS toward a Spiral Arm of M51

YURI NISHIMURA,^{1,2} YOSHIMASA WATANABE,^{3,4} NANASE HARADA,⁵ KOTARO KOHNO,^{1,6} AND SATOSHI YAMAMOTO^{7,6}

¹*Institute of Astronomy, The University of Tokyo, 2-21-1, Osawa, Mitaka, Tokyo 181-0015, Japan*

²*Chile Observatory, National Astronomical Observatory of Japan, 2-21-1, Osawa, Mitaka, Tokyo 181-8588, Japan*

³*Faculty of Pure and Applied Sciences, University of Tsukuba, Tsukuba, Ibaraki 305-8577, Japan*

⁴*Tomonaga Center for the History of the Universe, University of Tsukuba, Tsukuba, Ibaraki 305-8571, Japan*

⁵*Institute of Astronomy and Astrophysics, Academia Sinica, 11F of AS/NTUAstronomy-Mathematics Building, No.1, Sec. 4, Roosevelt Rd, Taipei 10617, Taiwan, R.O.C.*

⁶*Research Center for the Early Universe, The University of Tokyo, 7-3-1 Hongo, Bunkyo, Tokyo 113-0033*

⁷*Department of Physics, The University of Tokyo, 7-3-1 Hongo, Bunkyo, Tokyo 113-0033*

(Received February 12, 2019; Revised May 13, 2019; Accepted May 25, 2019)

Submitted to ApJ

ABSTRACT

Observations of various molecular lines toward a disk region of a nearby galaxy are now feasible, and they are being employed as diagnostic tools to study star-formation activities there. However, the spatial resolution attainable for a nearby galaxy with currently available radio telescopes is 10 – 1000 pc, which is much larger than the scales of individual star-forming regions and molecular cloud cores. Hence, it is of fundamental importance to elucidate which part of an interstellar medium such spatially-unresolved observations are tracing. Here we present sensitive measurements of the H₂CO (1₀₁ – 0₀₀) line at 72 GHz toward giant molecular clouds (GMCs) in the spiral arm of M51 using the NRO 45 m and IRAM 30 m telescopes. In conjunction with the previously observed H₂CO (2₀₂ – 1₀₁) and CS (2 – 1 and 3 – 2) lines, we derive the H₂ density of the emitting regions to be $(0.6 - 2.6) \times 10^4 \text{ cm}^{-3}$ and $(2.9 - 12) \times 10^4 \text{ cm}^{-3}$ for H₂CO and CS, respectively, by the non-LTE analyses, where we assume the source size of 0.8 – 1 kpc and the gas kinetic temperature of 10 – 20 K. The derived H₂ density indicates that the emission of H₂CO and CS is not localized to star-forming cores, but is likely distributed over an entire region of GMCs. Such widespread distributions of H₂CO and CS are also supported by models assuming lognormal density distributions over the 1 kpc region. Thus, contributions from the widespread less-dense components should be taken into account for interpretation of these molecular emission observed with a GMC-scale resolution. The different H₂ densities derived for H₂CO and CS imply their different distributions. We discuss this differences in terms of the formation processes of H₂CO and CS.

Keywords: galaxies: individual (M51) — galaxies: ISM — ISM: clouds — ISM: molecules — astro-chemistry

1. INTRODUCTION

Recently, molecular line observations in the millimeter and submillimeter wave regimes have become more and more popular in extragalactic studies (e.g., Aladro et al. 2015; Meier et al. 2015; Harada et al. 2018). Thanks to the advanced instrumental capabilities of single-dish

telescopes and interferometers, rotational spectral lines of various molecular species other than CO and its isotopologues can readily be detected in external galaxies. For instance, HCN and HCO⁺, which are often employed as dense-gas ($> 3 \times 10^4 \text{ cm}^{-3}$) tracers, have extensively been observed to reveal physical conditions of a molecular gas (e.g., Gao & Solomon 2004; Usero et al. 2015; Bigiel et al. 2016; Jiménez-Donaire et al. 2017). H₂CO and CS are also popularly observed to measure the gas density and temperature (e.g., Mauersberger &

Henkel 1989; Bayet et al. 2009; Mangum et al. 2013; Tang et al. 2017). Furthermore, molecular inventory is now being extended not only to bright central regions of galaxies but also to faint disk regions (e.g., Watanabe et al. 2014; Bigiel et al. 2016; Watanabe et al. 2019). However, the spatial resolution that can be achieved with currently available radio telescopes is 10 – 1000 pc even for nearby galaxies: an exception is the nearest galaxies such as the Large and Small Magellanic Clouds. This resolution is larger than typical sizes of star forming regions (~ 0.1 pc) and giant molecular clouds (GMCs, $\sim 1 - 10$ pc). To make a full use of molecular lines for physical and chemical diagnostics of disk regions in external galaxies, we need to know what parts of an interstellar medium the emission of the dense-gas tracers comes from. More specifically, it is important to validate whether the emission of each molecular species is exclusively localized to cloud cores or distributed also in the diffuse regime.

There are two approaches to this problem. One approach is to conduct a large-scale mapping observation toward Galactic GMCs with various molecular lines, and to evaluate a fraction of the emission coming from each part of GMCs (i.e., star forming cores, their envelopes, and cloud peripheries) for each molecular line when the line is observed with a large beam covering a whole GMCs. This approach is being conducted in several GMCs (Harada et al. 2019; Kauffmann et al. 2017; Nishimura et al. 2017; Pety et al. 2017; Watanabe et al. 2017). These studies indicate a significant contribution of the emission from less dense regions even for “dense-gas” tracers such as HCN, HCO⁺, and CS. The other approach, which is directly applicable for extragalactic sources, is to measure the gas density of the emitting region by multi-line observations. So far, multi-line observations have been conducted toward central regions of galaxies (e.g., Aladro et al. 2011b). On the other hand, such observations are very challenging toward disk regions because molecular lines are fainter (e.g., Usero et al. 2015; Bigiel et al. 2016). Consequently, the gas density traced by each molecular line is not fully understood particularly in disk regions. Nonetheless, the gas density in relatively quiescent disk regions is crucial for total understanding of star formation activities in a whole galaxy.

With this in mind, we have conducted very sensitive observations of the lowest transition line of H₂CO ($1_{01}-0_{00}$) toward a position in a spiral arm of the nearby spiral galaxy M51 ($D = 8.4$ Mpc; Vinkó et al. 2012). In conjunction with the previously observed $2_{02} - 1_{01}$ line (Watanabe et al. 2014), we evaluate the gas density of the emitting region of H₂CO by non-local thermal equi-

librium (LTE) analyses. The observation of the $1_{01}-0_{00}$ is essential to derive the gas density in a cold and less dense conditions. In addition, we derive the gas density of the emitting region of CS by using the existing data of the two CS lines ($J = 2 - 1$ and $3 - 2$; Watanabe et al. 2014). Based on the derived quantities, we consider the realistic H₂ density distribution within the telescope beam (~ 1 kpc). We also present implication of the derived results to formation processes of H₂CO and CS.

2. OBSERVATIONS AND RESULTS

Observations of the H₂CO ($1_{01} - 0_{00}$) line at 72.8379480 GHz were carried out with the 45 m radio telescope at the Nobeyama Radio Observatory (NRO 45 m) in 2014 May. The half power beam width is $\sim 22''$ at the observing frequency (72.72 GHz). We used the dual-polarization side-band separating (2SB) receiver T70. The system temperature ranged from 180 to 270 K. The sideband separation was typically 10 – 15 dB or better. The backend was the autocorrelator SAM45 (Kuno et al. 2011; Kamazaki et al. 2012). The frequency resolution and bandwidth are 488.28 kHz and 1600 MHz, respectively. The antenna temperature T_a^* was corrected for the main beam efficiency of 0.45 to obtain the main beam temperature T_{MB}^1 . We employed the position-switching mode, where the on-source integration time of each scan was set to be 20 seconds. The observed position was M51 P1 ($\alpha_{\text{J2000}} = 13^{\text{h}} 29^{\text{m}} 50^{\text{s}}.0$, $\delta_{\text{J2000}} = +47^\circ 11' 25''.0$), toward which Watanabe et al. (2014) conducted a spectral line survey in the 3 mm and 2 mm bands using the IRAM 30 m (Figure 1). The position is the brightest ¹²CO ($1 - 0$) peak in the spiral arm. It contains H α and Pa α emission spots and is also bright in 24 μm continuum emission, all of which indicate that star formation occurs inside (Schinnerer et al. 2010; Egusa et al. 2011). The off-source position was $10'$ away in azimuth from the on-source position. The telescope pointing was checked every 1–1.5 hours by observing nearby SiO maser sources (S-UMi and R-Cvn). The on-source integration time and the total observation time were 18 hr and 50 hr, respectively. The observation data were reduced with the NRO software *NEWSTAR*. In the analysis, we binned six successive channels of SAM45 to improve the signal-to-noise ratio. The resultant velocity resolution is 12.2 km s⁻¹ at 72 GHz. The rms noise temperature was 2 mK in the T_{MB} scale. Then, a baseline of the 5th-order polynomial was subtracted in the velocity range from -200 to 1200 km

¹ <http://www.nro.nao.ac.jp/~nro45mrt/html/prop/eff/eff2013.html>

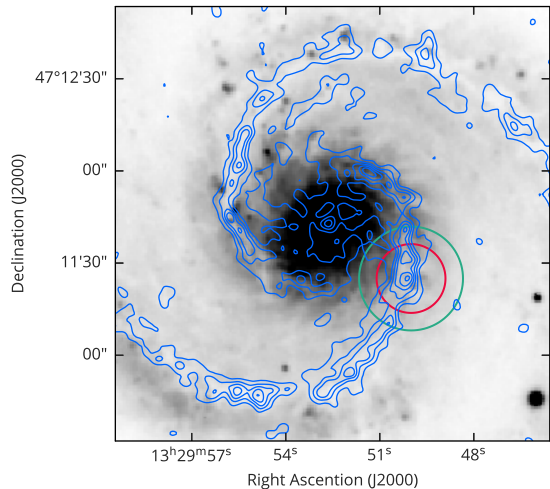


Figure 1. The observed position M51 P1 and the beam size of NRO 45 m (22.4'', red circle) and IRAM 30 m (33.8'', green circle) at the observing frequency of the H₂CO (1₀₁ – 0₀₀) line (72.72 GHz) overlaid on the *R*-band image (gray scale) by Hoopes et al. (2001) and the ¹²CO (1 – 0) integrated intensity (blue contours) by PAWS (Schinnerer et al. 2013). The contour levels are from 40 to 240 K km s⁻¹ at an interval of 40 K km s⁻¹.

s⁻¹. The line parameters were obtained by a single Gaussian fitting (Figure 2 top left), as summarized in Table 1.

The H₂CO (1₀₁ – 0₀₀) line was also observed with the IRAM 30 m telescope in 2018 January and May, as a part of the 70 GHz-band line survey toward the corresponding position in M51 (Y. Watanabe et al. in preparation). The observation was conducted by using the dual-sideband dual-polarization EMIR receiver² and the Fourier transform spectrometers. The half power beam width of IRAM 30 m at the frequency of the H₂CO (1₀₁ – 0₀₀) line is 33''.8. We performed a single Gaussian fitting to the observed line profile (Figure 2 middle left) and obtained the line parameters, as shown in Table 1.

In addition to the newly observed data, we use the existing data of the H₂CO (2₀₂ – 1₀₁) and CS (2 – 1 and 3 – 2) lines observed with IRAM 30 m (Watanabe et al. 2014). For these lines, we employ the line parameters reported by Watanabe et al. (2014).

3. NON-LTE ANALYSES

3.1. Non-LTE analyses using RADEX

In order to derive the gas density, we conduct non-LTE analyses of the observed data. We use the publicly available code RADEX (van der Tak et al. 2007) with collisional rate coefficients of H₂CO (Wiesenfeld & Faure 2013) and CS (Lique et al. 2006). RADEX requires five input parameters to calculate the intensities of molecular lines: background temperature, line width, column density of a given species, gas kinetic temperature, and H₂ density. We select the H₂ density and the column density as adjustable parameters to reproduce the observed integrated intensities.

Prior to the analyses, the intensity of each molecular line is corrected for the beam dilution effect. Beam dilution is caused by the coupling between the source and the telescope beam, as $T_B = [(\theta_s^2 + \theta_b^2)/\theta_s^2]T_{MB}$, where T_B is the source-averaged brightness temperature, θ_s is the source size, θ_b is the beam size of the telescope, and T_{MB} is the measured main-beam temperature. For H₂CO, the source size is derived to be 25'' (1 kpc) by using the two measurements of the H₂CO (1₀₁ – 0₀₀) line with the different telescope beams (22''.4 and 33''.8). Such a wide distribution seems likely, because H₂CO is ubiquitously detected toward Galactic clouds (e.g., ~ 80% of 262 Galactic radio sources; Downes et al. 1980). For CS, we assume the source size on the basis of the interferometric observations in the literature: Watanabe et al. (2016) mapped the same region in the CS (2 – 1) line with the Combined Array for Research in Millimeter-wave Astronomy (CARMA) at a ~ 6'' resolution. The CS emission has a distribution extending along the spiral arm with a size of ~ 20'' (0.8 kpc). The flux resolved out by the interferometer (missing flux) is estimated to be ~ 30% by comparing with the flux obtained with IRAM 30 m (Watanabe et al. 2014). We should keep in mind that the flux from the extended component may contribute appreciably in the single dish observations. Hence, we assume the two source sizes of 25'' and 20'' for both H₂CO and CS in the following analyses.

The assumptions in the analyses are as follows: we adopt the cosmic microwave background temperature of 2.73 K. For the line width, we use 37 km s⁻¹ for H₂CO and 48 km s⁻¹ for CS, taking an average of the observed values (Table 1). As for the gas kinetic temperature, Schinnerer et al. (2010) derive it to be 16 – 20 K by a large velocity gradient (LVG) modeling of the line intensity ratios of ¹²CO (1 – 0), ¹²CO (2 – 1) and ¹³CO (1 – 0). Hence, we assume a somewhat wide range of the temperature, i.e., 10, 15, and 20 K. We run the RADEX code with the above parameters, where model grids of the H₂ density and the column density are set to 30 values logarithmically spaced from 10² to 10⁶ cm⁻³ and 30

² <http://www.iram.es/IRAMES/mainWiki/EmirforAstronomers>

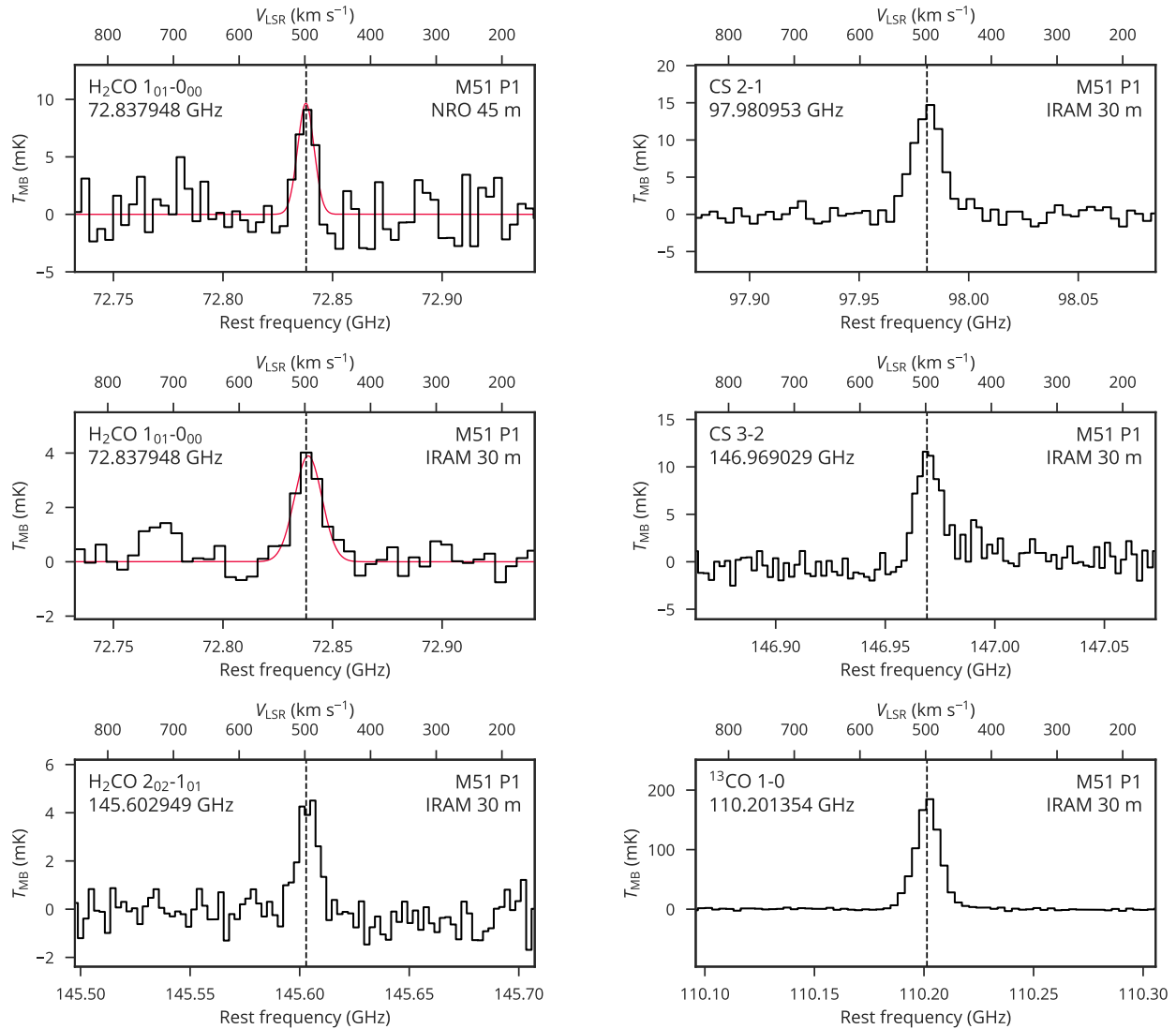


Figure 2. The H_2CO ($1_{01} - 0_{00}$) spectrum at 72.83798 GHz toward M51 P1 obtained with NRO 45 m (*top left*) and IRAM 30 m (*middle left*). The red curves show the results of a single Gaussian fit. The spectra of H_2CO ($2_{02} - 1_{01}$; *bottom left*), CS ($2 - 1$; *top right*), CS ($3 - 2$; *middle right*), and ^{13}CO ($1 - 0$; *bottom right*) obtained by Watanabe et al. (2014) are also shown for comparison. The dashed vertical lines indicate the LSR velocity of 498 km s^{-1} . The rest frequency is represented by assuming the LSR velocity of 498 km s^{-1} for all the panels. Note that the temperature scale of the spectrum is different from panel to panel.

values logarithmically spaced from 10^{10} to 10^{15} cm^{-2} , respectively.

As a result, we successfully constrain the H_2 densities of the emitting regions and the column densities from the observed integrated intensities and their ratios for some combinations of the assumed parameters. The derived H_2 densities and column densities are listed in Table 2. In Table 2, we also report the optical depths for the H_2CO ($1_{01} - 0_{00}$) and CS ($2 - 1$) lines for reference. Figure 3 shows an example of a plausible parameter set. Depending on the gas kinetic temperature (10 – 20 K) and the source size (20 – 25 $''$), the H_2 density spans from 5.7×10^3 to $2.6 \times 10^4 \text{ cm}^{-3}$ for H_2CO and 2.9×10^4

to $1.2 \times 10^5 \text{ cm}^{-3}$ for CS. The column densities are in the range of $(3.3 - 9.0) \times 10^{12} \text{ cm}^{-2}$ for H_2CO^3 and $(0.8 - 1.7) \times 10^{13} \text{ cm}^{-2}$ for CS. Note that the observed intensities for H_2CO cannot be reproduced with any set of the H_2 density and the column density, if the gas kinetic temperature is assumed to be of 15 and 20 K with the source size of 20 $''$.

³ Note that this is just for para- H_2CO . If we assume the ortho-to-para ratio to be 3 (the statistical value), the total (ortho and para) column density of H_2CO is in the range of $(1.3 - 3.6) \times 10^{13} \text{ cm}^{-2}$.

Table 1. Observed Line Parameters

Molecule	Transition	Frequency (GHz)	E_{up} (K)	$\int T_{\text{MB}} dv$ (K km s $^{-1}$)	FWHM (km s $^{-1}$)	v_{LSR} (km s $^{-1}$)	$T_{\text{MB peak}}$ (mK)	θ_{beam} ($''$)	Reference
H ₂ CO	1 ₀₁ – 0 ₀₀	72.837948	3.5	0.30 ± 0.09	29 ± 19	498 ± 3	10 ± 6	22.4	This work
				0.19 ± 0.03	49 ± 17	495 ± 7	4 ± 1	33.8 ^a	Watanabe et al. (in prep.)
H ₂ CO	2 ₀₂ – 1 ₀₁	145.602949	10.5	0.14 ± 0.03	34 ± 3	495 ± 1	4 ± 1	16.9 ^a	Watanabe et al. (2014)
CS	2 – 1	97.980953	7.1	0.68 ± 0.08	52 ± 3	497 ± 1	13 ± 2	25.1 ^a	Watanabe et al. (2014)
CS	3 – 2	146.969029	14.1	0.4 ± 0.1	45 ± 4	495 ± 2	9 ± 3	16.7 ^a	Watanabe et al. (2014)

^a The half power beam width of IRAM 30 m at the given frequency ν is $2460'' \cdot (\nu/\text{GHz})^{-1}$.

NOTE—The uncertainties are 3σ .

Table 2. Results of RADEX non-LTE modeling (single density component)

Molecule	Assumed		Derived			Comments
	θ_{source} ($''$)	T_{kin} (K)	N_{mol} (cm $^{-2}$)	τ	n_{H_2} (cm $^{-3}$)	
(1)	(2)	(3)	(4)	(5)	(6)	(7)
H ₂ CO	25	10	3.3×10^{12}	0.014	2.6×10^4	See Figure 3
		15	5.0×10^{12}	0.024	1.1×10^4	
	20	20	7.1×10^{12}	0.038	5.7×10^3	
		10	9.0×10^{12}	0.048	1.1×10^4	
		15	–	–	–	^a
CS	25	10	8.1×10^{12}	0.014	1.2×10^5	See Figure 3
		15	8.9×10^{12}	0.016	6.4×10^4	
	20	20	1.0×10^{13}	0.019	4.3×10^4	
		10	1.2×10^{13}	0.022	9.5×10^4	
		15	1.4×10^{13}	0.028	4.7×10^4	
	20	1.7×10^{13}	0.036	2.9×10^4		

NOTE—Columns are: (1) molecular species, (2) assumed source size, (3) assumed gas kinetic temperature, (4) derived column density, (5) derived optical depth of the 1₀₁ – 0₀₀ and 2 – 1 lines for H₂CO and CS, respectively, (6) derived H₂ density of the emitting region, (7) other remarks.

^a The assumed parameter set of the gas kinetic temperature and the source size does not reproduce the observed intensities at any set of the H₂ density and the column density.

3.2. The H₂ densities for the emitting regions of H₂CO and CS

As described in the previous section, the H₂ densities for the emitting region of H₂CO and CS are evaluated to be $(0.6 - 2.6) \times 10^4$ cm $^{-3}$ and $(2.9 - 12) \times 10^4$ cm $^{-3}$, respectively. It seems reasonable that the derived H₂ densities for the emitting region of H₂CO (1₀₁ – 0₀₀) and CS (2 – 1) are higher than that derived for ¹³CO (1–0) and ¹²CO (1–0, 2–1) ($120 - 240$ cm $^{-3}$; Schinnerer et al. 2010), because the H₂CO and CS lines have higher critical densities than the CO isotopologue lines. Indeed, the derived densities are similar to the effective critical

densities (H₂CO (1₀₁ – 0₀₀): 3×10^4 cm $^{-3}$, CS (2 – 1): 5×10^4 cm $^{-3}$ at 15 K; Shirley 2015)⁴.

As expected, the derived density in the spiral arm of M51 is lower than that in the central region of M51 derived by the HCN (1 – 0) and ¹³CO (1 – 0) lines (> 100 K and $\sim 10^5$ cm $^{-3}$; Matsushita et al. 1998), where a heavily-obscured AGN associated with radio jet and ion-

⁴ The effective critical density is the density at which collisional and radiative processes balance each other under taking radiative trapping into account. It depends on the molecular column density. The above mentioned values are scaled to the derived column densities by using Eq. (13) of Shirley (2015).

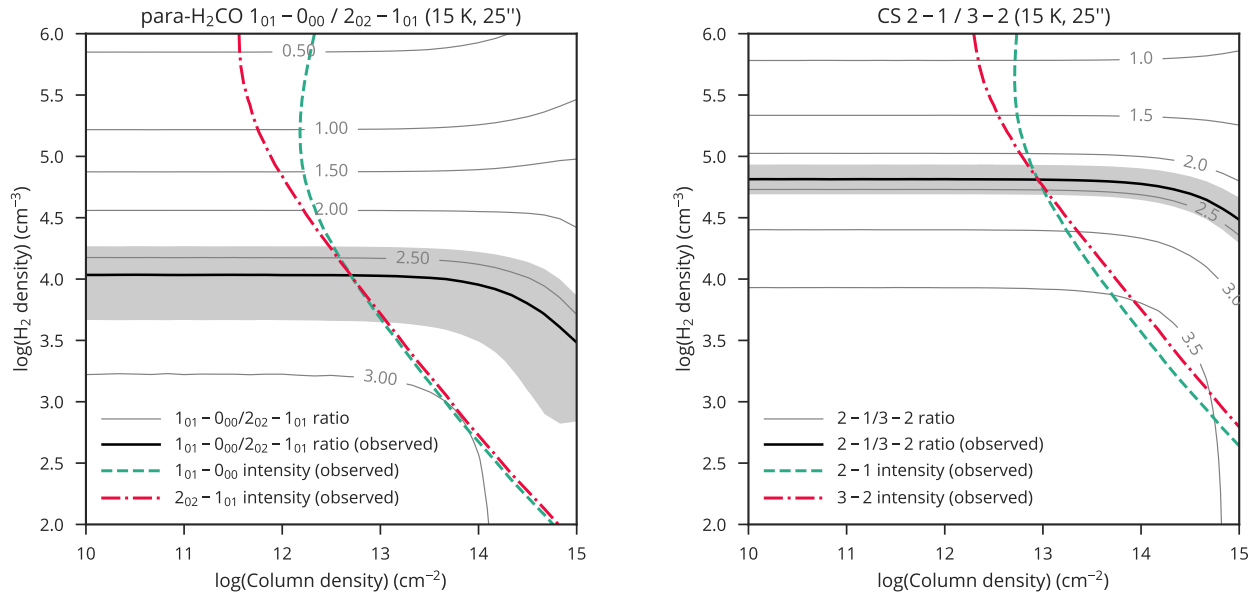


Figure 3. RADEX non-LTE model assuming a single density component. Model grids are the column density and the H₂ density. (*left*) The H₂CO 1₀₁ - 0₀₀/2₀₂ - 1₀₁ integrated intensity ratio (black solid), the 1₀₁ - 0₀₀ integrated intensity (green dashed), and the 2₀₂ - 1₀₁ integrated intensity (red dash-dotted). (*right*) The CS 2 - 1/3 - 2 integrated intensity ratio (black solid), the 2 - 1 integrated intensity (green dashed), and the 3 - 2 integrated intensity (red dash-dotted). The uncertainties of the line ratio (1 σ) are shaded in gray. A case for the gas kinetic temperature of 15 K is shown.

ized/molecular outflows exists (e.g., Kohno et al. 1996; Matsushita et al. 2007). This result seems reasonable, because the observed position in the spiral arm is, unlike the central region, free from nuclear jets and/or compression by supernova-driven winds.

Although the H₂ densities of the emitting region of H₂CO and CS are higher than that of CO isotopologues, they seem to be widely distributed over the GMCs. If H₂CO and CS are localized to dense clumps and are deficient in diffuse parts of clouds, the derived gas densities would be higher. The similarity of the derived H₂ densities and the effective critical densities may imply that H₂CO and CS reside in the wide ranges of density from that well below to that well above the effective critical densities. Hence, both H₂CO and CS are not localized to dense star-forming cores (< 0.1 pc and > 10⁵ cm⁻³), but rather reside in a considerably large fraction of the GMCs. Our result indicates that H₂CO and CS in relatively less dense parts of molecular clouds mainly contribute to their emission in the 3 mm and 2 mm regions. This result should be considered in interpretation of molecular emissions in a disk region of a galaxy observed with a molecular-cloud-scale beam.

4. IMPLICATIONS FOR REALISTIC DENSITY DISTRIBUTIONS

Both theoretical and observational studies have pointed out that molecular clouds comprise a wide range of gas densities from diffuse to dense ones. As

a functional form of density distribution, lognormal functions are often predicted by turbulent theories (e.g., Padoan & Nordlund 2002). Milky Way observations are basically consistent with these theories, but it is sometimes pointed out that power laws better describe distributions at high densities (e.g., Lombardi et al. 2015). To explore the density distribution from spatially-unresolved observations toward external galaxies, Leroy et al. (2017) demonstrated that a proper set of molecular line intensities is useful to probe underlying distributions. Given that H₂CO and CS are widely distributed over the molecular clouds, we here consider the H₂ density distribution within the observed 1 kpc beam, assuming a lognormal distribution with and without a power law tail as employed by Leroy et al. (2017).

4.1. Modeling of line intensity and emissivity

Prior to integrating the intensities for a wide range of H₂ density, we run the RADEX code to calculate line intensities of the H₂CO and CS transitions at each density. As the input parameters for RADEX, we adopt the same values as Section 3: the background temperature of 2.73 K, the gas kinetic temperature T_{kin} of 10 and 15 K⁵, and line widths of 37 and 48 km s⁻¹ for H₂CO and

⁵ Here, we do not consider the case of $T_{\text{kin}} = 20$ K. At 20 K, the level populations of the 0₀₀ and 1₀₁ levels of H₂CO are inverted in a certain range of the H₂ density and a certain range of the column

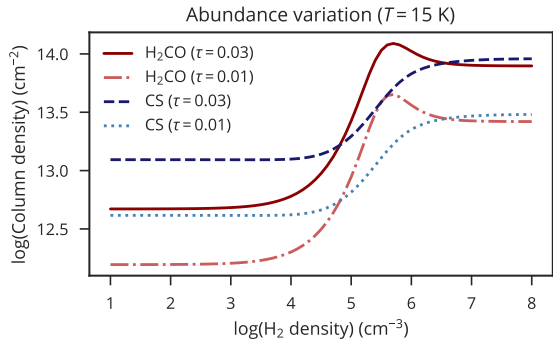


Figure 4. Variation of the column densities of H₂CO and CS within the model H₂ density distribution under the fixed optical depth for the lower-*J* transition. Here, we fix the gas kinetic temperature to be 15 K. Cases for the optical depths of $\tau = 0.03$ and 0.01 are shown. Note that these results do not take any chemical processes into account.

CS, respectively. The H₂ densities are 70 values logarithmically spaced in the range of from 10^1 to 10^8 cm⁻³. Following Leroy et al. (2017), we adjust the molecular column density to keep the optical depth fixed. Based on the estimation in Section 3.1, we set the optical depth of the lower-*J* transitions to be $\tau = 0.03$ and 0.01. The optical depth of higher-*J* transition is calculated consistently from the lower-*J* transition. Under the fixed optical depth, the column density varies as a function of H₂ density (Figure 4). However, this abundance variations of H₂CO and CS may be underestimated, because chemical models predict even larger variations along H₂ density (e.g., Harada et al. 2019). The abundance variations could be improved by taking chemical processes into account in future work.

For each density step, we calculate emissivity ϵ . Here, emissivity is defined as the intensity *I* divided by the H₂ column density N_{H_2} . For consistency with Leroy et al. (2017), the column density of H₂ is calculated by dividing the column density of emitting molecule N_{mol} , by the fractional abundance of the molecule X_{mol} . Then, the emissivity is calculated as $\epsilon = I/N_{\text{mol}}X_{\text{mol}}^{-1}$. The fractional abundance is adjusted to be 10^{-9} for both H₂CO and CS so that $N_{\text{mol}}X_{\text{mol}}^{-1}$ is roughly comparable with the reported column density of $N_{\text{H}_2} = (2.3 - 3.3) \times 10^{22}$ cm⁻² (Schinnerer et al. 2013).

4.2. Lognormal and power law distributions

Following Leroy et al. (2017), we consider two kinds of functional form for the H₂ density distribution: lognormals with and without a power law tail at high density.

density. To keep the optical depth fixed, the column density of H₂CO has to be discontinuous as a function of H₂ density. Such a discontinuity of column density is not realistic.

Lognormal distributions are described by:

$$dP(\ln n') \propto \exp\left(-\frac{(\ln n' - \overline{\ln n'})^2}{2\sigma^2}\right) d\ln n',$$

where dP is the fraction of cells in a logarithmic step $d\ln n'$, $n' = n_{\text{H}_2}/n_0$ is the H₂ density normalized by the mean H₂ density n_0 , and σ is the rms dispersion of the distribution. The distribution peaks at the mean of the logarithm of the density $\overline{\ln n'}$, which is determined by the relation: $\overline{\ln n'} = -\sigma^2/2$. As the lognormal distribution is a result from isothermal supersonic turbulence, σ is related to the turbulent Mach number \mathcal{M} : $\sigma^2 = \ln(1 + \mathcal{M}^2/4)$ (for more details, see Padoan & Nordlund 2002). For easier comparison with Leroy et al. (2017), we use \log_{10} , so that σ is represented in dex. To incorporate a power law tail, we employ the formulation:

$$dP(\ln n') \propto \exp(\alpha \ln n') \text{ for } n' > n'_{\text{thresh}},$$

where the power law index is taken to be $\alpha = -1.5$, and the threshold for the power law tail to be $\ln n'_{\text{thresh}} = 3.8$ (Federrath & Klessen 2013). The model grids of the mean H₂ density and the width of distribution are set to be logarithmically spaced 40 points in the range of $n_0 = 10^2 - 10^6$ cm⁻³, and linearly spaced 8 points in the range of $\sigma = 0.4 - 1.2$, respectively, for each of lognormal distributions with and without power law tails.

4.3. Realistic H₂ density distributions

For each H₂ density distribution, we derive the beam averaged emissivity by summing up the emissivity along the axis of H₂ density (Leroy et al. 2017):

$$\langle \epsilon \rangle = \frac{\int n_{\text{H}_2} P(n_{\text{H}_2}) \epsilon(n_{\text{H}_2}, T_{\text{kin}}, \tau) dn_{\text{H}_2}}{\int n_{\text{H}_2} P(n_{\text{H}_2}) dn_{\text{H}_2}}.$$

We calculate the line intensities integrated over the 1 kpc beam, by multiplying the H₂ column density of $N_{\text{H}_2} = 3 \times 10^{22}$ cm⁻² (Schinnerer et al. 2013) to the beam averaged emissivity $\langle \epsilon \rangle$. This causes minor inconsistency between N_{H_2} and $N_{\text{mol}}X_{\text{mol}}^{-1}$, because $N_{\text{mol}}X_{\text{mol}}^{-1}$ slightly vary within the model distribution. As we do not know the exact fractional abundances of molecules at a specific H₂ density, we employ this simplest assumption.

By comparing the modeled line intensities and their ratios with observed ones, the parameters of the density distribution are constrained as summarized in Table 3. In Figure 5, we show the model grids for plausible parameter sets. Figure 6 illustrates the distribution of volume, mass, emissivity and emission for each plausible parameter sets. Compared with pure lognormal distributions, the model with a power law tail tends to

show the lower mean H_2 density and the narrower width of distribution. The mean H_2 density is in a range of $n_0 = 130 - 6600 \text{ cm}^{-3}$. This seems reasonable, because the range overlaps to $120 - 240 \text{ cm}^{-3}$, which is derived from ^{12}CO and ^{13}CO observations (Schinnerer et al. 2013). The width of distribution, on the other hand, is in the range of $\sigma = 0.4 - 0.9$, which corresponds to $\mathcal{M} = 2.3 - 18$ in turbulent Mach number. This range almost falls on the smallest case of the typical value ($5 - 100$) for spiral and starburst galaxies (Leroy et al. 2016).

Note that, in any density distribution, we cannot simultaneously reproduce the observed intensity of H_2CO and CS. This would probably originate from the fixed kinetic temperature and, most notably, the arbitrary assumption for their abundances to keep the optical depth fixed. In the next section, we discuss chemical processes to form H_2CO and CS, which may differentiate their distribution. Implementing more realistic molecular abundance variation is awaited for future study.

Finally, we discuss the median intensity for emission $n_{\text{med}}^{\text{emis}}$, which is defined by the H_2 density below which 50% of the line emission emerges (Leroy et al. 2017). Here, we consider the lines of lower- J transitions, i.e., $1_{01} - 0_{00}$ for H_2CO and $2 - 1$ for CS. The modeled values of the median intensity for emission are shown in Table 3. These are consistent with the H_2 densities of the emitting regions derived in Section 3. This supports the picture suggested in Section 3.2 that H_2CO and CS are present in a wide range of H_2 density.

5. IMPLICATIONS FOR CHEMICAL PROCESSES

Formation and destruction processes of molecules depend on the physical conditions. The relatively low density ($\sim 10^4 \text{ cm}^{-3}$) of the emitting regions of H_2CO and CS suggests that these molecules are not localized to dense and hot regions associated with active star formation. In the following subsections, implications of this result to the chemical processes of H_2CO and CS are discussed.

5.1. H_2CO

In general, both grain surface reactions and gas phase reactions are thought to contribute to the production of H_2CO . Theoretical models and laboratory experiments suggest that successive hydrogenation of CO in icy mantles of dust grains followed by subsequent liberation into the gas phase by thermal and/or non-thermal desorption is the dominant process ($\text{CO} \rightarrow \text{HCO} \rightarrow \text{H}_2\text{CO}$; Watanabe & Kouchi 2002), although the gas phase formation can produce some abundance of H_2CO (e.g., Soma et al. 2018).

In our case, widespread H_2CO in relatively less dense gas would not originate from thermal desorption. As the desorption temperature is as high as 40 K, the thermal desorption is restricted in small hot and dense regions around newly born stars (i.e., hot cores) and/or outflow shocked regions. Then, the non-thermal desorption should mainly be responsible for the liberation of H_2CO formed in ice mantles. This is supported by the previous observation of CH_3OH toward this position of M51 (Watanabe et al. 2014, 2016). According to them, the distribution of CH_3OH is widespread over a 100 pc scale. CH_3OH is formed on grain surface by further hydrogenation of H_2CO ($\text{H}_2\text{CO} \rightarrow \text{CH}_3\text{O} \rightarrow \text{CH}_3\text{OH}$; Watanabe & Kouchi 2002), whereas it is not efficiently produced by the gas-phase reactions (Geppert et al. 2006). Therefore, a widespread CH_3OH suggests its non-thermal desorption, and in this case, H_2CO should also be liberated. As for the non-thermal desorption processes, sputtering of molecules in large-scale shocks such as spiral shocks and cloud-cloud collisions as well as temporal heating of dust grains by cosmic rays and liberation assisted by surplus reaction energy in formation of molecules are proposed (e.g., Hasegawa & Herbst 1993; Garrod et al. 2007). It is worth noting that desorption by UV photons can also work for H_2CO but not for CH_3OH (Martín-Doménech et al. 2016).

The abundance ratio $\text{CH}_3\text{OH}/\text{H}_2\text{CO}$ in M51 P1 is evaluated to be 1.5 by using the column density of H_2CO obtained in this study and that of CH_3OH reported by Watanabe et al. (2014). Here, the ortho-to-para ratio of H_2CO is assumed to be the statistical value of 3, and the line intensity of CH_3OH is corrected for the source size of $25''$ for the fair comparison. The $\text{CH}_3\text{OH}/\text{H}_2\text{CO}$ ratio in various Galactic objects varies by two orders of magnitude from 0.3 (e.g., ρ Oph A D-peak; Bergman et al. 2011) to 24 (e.g., NGC 6334 IRS1; van der Tak et al. 2000). The difference may originate from different hydrogenation of CO in ice mantles and/or different contribution of the gas phase production. The ratio in M51 P1 is just in the middle of this range. It is not very different from those in the other external galaxies M82 (1.1; Aladro et al. 2011a) and NGC 253 (5.2; Martín et al. 2006), although the physical condition of M51 P1 is much different from these two sources.

5.2. CS

It is well known that CS is ubiquitous in various interstellar sources including diffuse clouds (e.g., Lucas & Liszt 2002). Gas-phase reactions are thought to be important in its production, and hence, CS can be formed under the less dense condition of M51 P1. According to the interferometric observation by Watanabe et al.

Table 3. Results of RADEX non-LTE modeling (lognormal distribution with and without power law tail)

Molecule	Assumed				Derived			Comments
	θ_{source} (")	T_{kin} (K)	τ	Distribution	n_0 (cm^{-3})	σ (dex)	$n_{\text{med}}^{\text{emis}}$ (cm^{-3})	
(1)	(2)	(3)	(4)	(5)	(6)	(7)	(8)	(9)
H ₂ CO	25	10	0.01	lognormal	–	–	–	^a
			0.03	lognormal	–	–	–	^a
	20	15	0.01	lognormal	1.3×10^2	0.7	5.0×10^3	See Figure 5 and 6
			0.03	lognormal	1.3×10^2	0.7	5.0×10^3	
		10	0.01	lognormal	6.5×10^2	0.5	6.3×10^3	^a
			0.03	lognormal	6.5×10^2	0.5	6.3×10^3	
15	0.01	lognormal	–	–	–	^a		
	0.03	lognormal	–	–	–	^a		
CS	25	10	0.01	lognormal	6.8×10^2	0.9	7.9×10^4	See Figure 5 and 6
			0.03	lognormal	7.4×10^2	0.9	7.9×10^4	
	20	15	0.01	lognormal	1.2×10^3	0.7	4.0×10^4	
			0.03	lognormal	1.2×10^3	0.7	4.0×10^4	
		10	0.01	lognormal	4.0×10^3	0.7	6.3×10^4	
			0.03	lognormal	4.1×10^3	0.7	6.3×10^4	
15	0.01	lognormal	5.2×10^3	0.5	3.2×10^4			
	0.03	lognormal	5.3×10^3	0.5	3.2×10^4			
H ₂ CO	25	10	0.01	lognormal+tail	5.6×10^2	0.5	3.2×10^3	See Figure 5 and 6
			0.03	lognormal+tail	5.7×10^2	0.5	3.2×10^3	
	20	15	0.01	lognormal+tail	5.1×10^2	0.4	2.0×10^3	
			0.03	lognormal+tail	5.1×10^2	0.4	2.0×10^3	
		10	0.01	lognormal+tail	1.2×10^3	0.4	4.0×10^3	
			0.03	lognormal+tail	1.2×10^3	0.4	4.0×10^3	
15	0.01	lognormal+tail	–	–	–	^a		
	0.03	lognormal+tail	–	–	–	^a		
CS	25	10	0.01	lognormal+tail	3.1×10^3	0.6	4.0×10^4	See Figure 5 and 6
			0.03	lognormal+tail	3.2×10^3	0.6	4.0×10^4	
	20	15	0.01	lognormal+tail	3.2×10^3	0.5	2.5×10^4	
			0.03	lognormal+tail	3.2×10^3	0.5	2.5×10^4	
		10	0.01	lognormal+tail	6.6×10^3	0.5	5.0×10^4	
			0.03	lognormal+tail	6.7×10^3	0.5	5.0×10^4	
15	0.01	lognormal+tail	6.5×10^3	0.5	2.5×10^4			
	0.03	lognormal+tail	6.6×10^3	0.5	2.5×10^4			

NOTE—Columns are: (1) molecular species, (2) assumed source size, (3) assumed gas kinetic temperature, (4) assumed optical depth of the $1_{01} - 0_{00}$ and $2 - 1$ lines for H₂CO and CS, respectively, (5) assumed density distribution, (6) mean H₂ density for the lognormal part of the density distribution, (7) dispersion in the lognormal part of the density distribution, (8) median density below which 50% of the emission of the lower- J transition emerges, (9) other remarks.

^a The assumed parameter set of the gas kinetic temperature, the source size, and the optical depth does not reproduce the observed intensities at any set of the mean H₂ density and the width of distribution.

(2016), the distribution of CS is slightly more extended than CH₃OH in M51 P1. Hence, the different spatial distribution would originate from the contribution of the gas-phase production of CS as oppose to the grain-surface production of CH₃OH. The slightly different H₂ densities derived from H₂CO and CS would suggest the different production mechanism.

The CS/H₂CO ratio is evaluated to be 0.5 in M51 P1. The ratios in various Galactic sources range from 0.4 (e.g., Galactic diffuse clouds; Liszt et al. 2006) to 1.6 (e.g., IRAS 16293-2422; Blake et al. 1994; van Dishoeck

et al. 1995), and hence, the ratio in M51 P1 falls in this range. It is worth noting that the ratios are 1.8 in M82 (Aladro et al. 2011a) and 1.6 (180 km s⁻¹ component) – 2.9 (285 km s⁻¹ component) in NGC 253 (Martín et al. 2006), which also agree with the ratio in M51 P1 by a factor of a few, as in the case for the CH₃OH/H₂CO ratio. We need more samples to examine whether this is just by chance or by some chemical reasons.

These results provide us with an additional support that the molecular composition averaged over a few 10 – 100 pc scale observed with single dish telescopes in

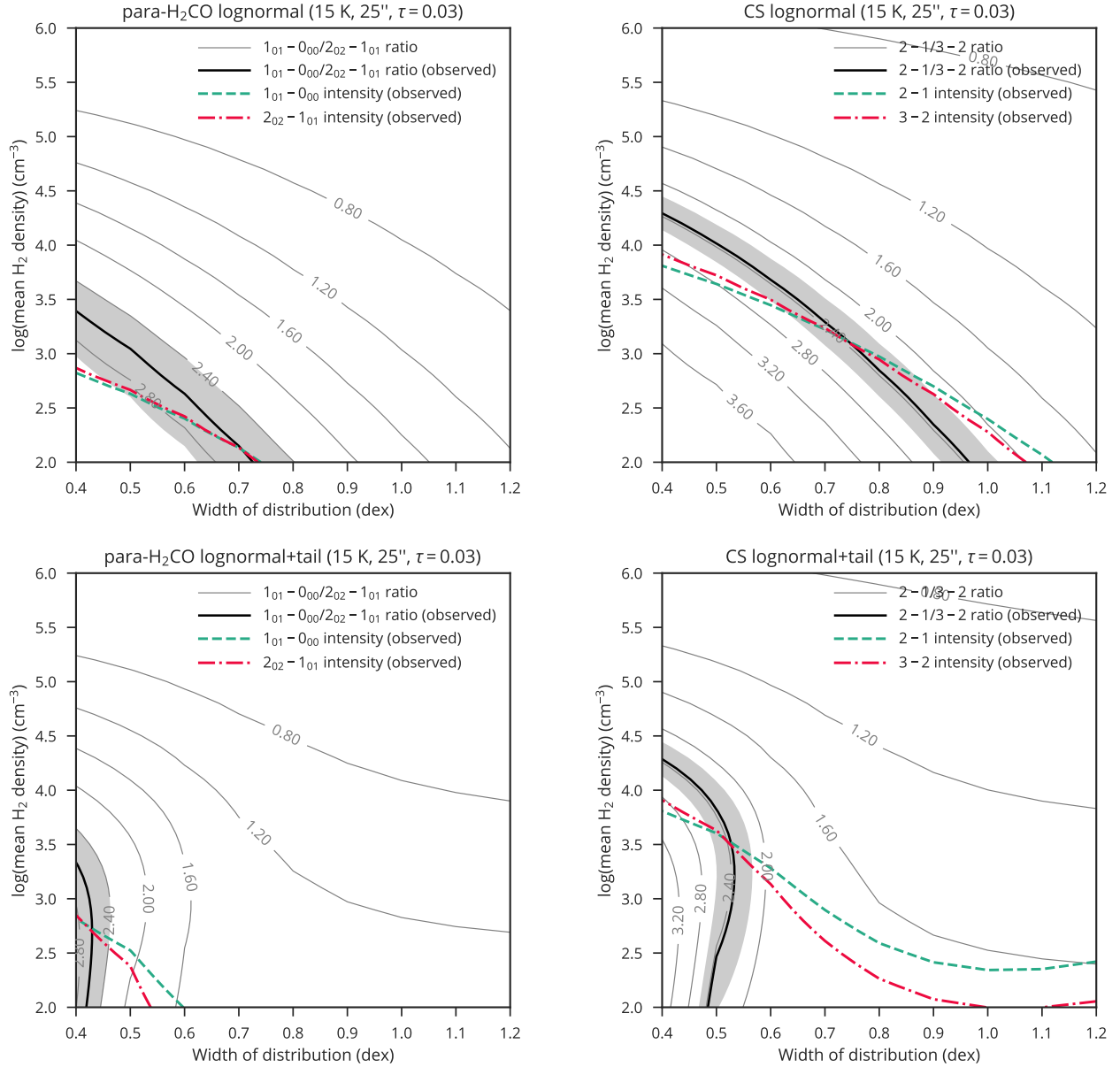


Figure 5. As in Figure 3, but assuming the lognormal distribution of the H₂ densities with (*upper panels*) and without (*lower panels*) a power law tail at high density. Model grids are the mean H₂ density and the rms dispersion of the lognormal distribution. Here, we adopt the fixed optical depth of lower- J transitions ($\tau = 0.03$). In the cases with the power law tail, the intensity ratio patterns differ from the pure lognormal distributions at large widths of the distribution.

the 3 mm wavelength range mostly reflects that of the widespread gas rather than that affected by local star formation activities, as inferred by the previous studies of Galactic GMCs (Nishimura et al. 2017; Watanabe et al. 2017). According to them, the 3 mm-band spectra averaged over a GMC scale (the 39 pc \times 47 pc area in W51; Watanabe et al. 2017 and the 9 pc \times 9 pc area in W3(OH); Nishimura et al. 2017) are similar to the spectra of diffuse cloud peripheries rather than those of dense regions. This trend is also supported by the chemical model calculation by Harada et al. (2019).

6. SUMMARY

We study the gas densities of the emitting regions of the two commonly-observed molecular species H₂CO and CS in a 1 kpc region in the spiral arm of M51. We have conducted sensitive observations of the H₂CO (1₀₁ - 0₀₀) line using the NRO 45 m and IRAM 30 m telescopes. Combining our new data with the data of H₂CO (2₀₂ - 1₀₁) and CS (2 - 1 and 3 - 2) previously reported by Watanabe et al. (2014), we find that the emitting regions of H₂CO and CS have the relatively low

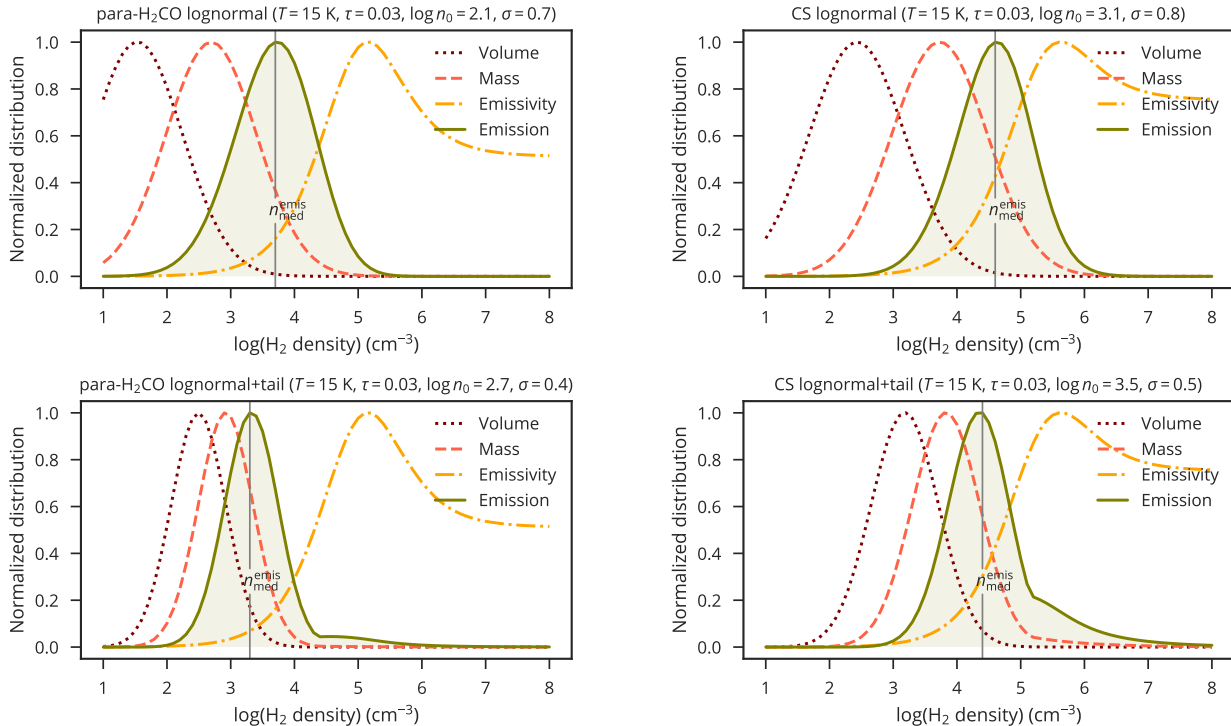


Figure 6. Model distributions of H_2 density by volume (dotted) and mass (dashed), molecular emissivity (dash-dotted), and emission (solid) for plausible parameter sets in Figure 5. Each distribution is normalized to its peak value at any H_2 density. Vertical lines indicate the median H_2 density for molecular emission. Here, molecular emissivity is defined as emission per unit column density.

H_2 density of $(0.6 - 2.6) \times 10^4 \text{ cm}^{-3}$ and $(2.9 - 12) \times 10^4 \text{ cm}^{-3}$, respectively. This indicates that these two species are not concentrated in the star-forming cores, but are widely distributed over the GMCs. Models assuming the lognormal H_2 density distribution with fixed optical depths also support this picture. The different H_2 densities derived for H_2CO and CS imply their different distributions, and probably different formation processes.

We are grateful to the anonymous referee for his/her comments and suggestions to improve the paper. We thank the staff of the NRO 45 m telescope for excellent support. This work is supported by NAOJ ALMA Scientific Research Grant Number 2017-06B and JSPS KAKENHI Grant Number JP18K13577.

Facility: NRO 45 m

Software: Newstar

REFERENCES

- Aladro, R., Martín, S., Martín-Pintado, J., et al. 2011a, *A&A*, 535, A84
- Aladro, R., Martín-Pintado, J., Martín, S., Mauersberger, R., & Bayet, E. 2011b, *A&A*, 525, A89
- Aladro, R., Martín, S., Riquelme, D., et al. 2015, *A&A*, 579, A101
- Bayet, E., Aladro, R., Martín, S., Viti, S., & Martín-Pintado, J. 2009, *ApJ*, 707, 126
- Bergman, P., Parise, B., Liseau, R., & Larsson, B. 2011, *A&A*, 527, A39
- Bigiel, F., Leroy, A. K., Jiménez-Donaire, M. J., et al. 2016, *ApJ*, 822, L26
- Blake, G. A., van Dishoeck, E. F., Jansen, D. J., Groesbeck, T. D., & Mundy, L. G. 1994, *ApJ*, 428, 680
- Downes, D., Wilson, T. L., Bieging, J., & Wink, J. 1980, *A&AS*, 40, 379
- Egusa, F., Koda, J., & Scoville, N. 2011, *ApJ*, 726, 85
- Federrath, C., & Klessen, R. S. 2013, *ApJ*, 763, 51
- Gao, Y., & Solomon, P. M. 2004, *ApJ*, 606, 271
- Garrod, R. T., Wakelam, V., & Herbst, E. 2007, *A&A*, 467, 1103
- Geppert, W. D., Hamberg, M., Thomas, R. D., et al. 2006, *Faraday Discussions*, 133, 177
- Harada, N., Nishimura, Y., Watanabe, Y., et al. 2019, *ApJ*, 871, 238

- Harada, N., Sakamoto, K., Martín, S., et al. 2018, *ApJ*, 855, 49
- Hasegawa, T. I., & Herbst, E. 1993, *MNRAS*, 261, 83
- Hoopes, C. G., Walterbos, R. A. M., & Bothun, G. D. 2001, *ApJ*, 559, 878
- Jiménez-Donaire, M. J., Bigiel, F., Leroy, A. K., et al. 2017, *MNRAS*, 466, 49
- Kamazaki, T., Okumura, S. K., Chikada, Y., et al. 2012, *PASJ*, 64, 29
- Kauffmann, J., Goldsmith, P. F., Melnick, G., et al. 2017, *A&A*, 605, L5
- Kohno, K., Kawabe, R., Tosaki, T., & Okumura, S. K. 1996, *ApJL*, 461, L29
- Kuno, N., Takano, S., Iono, D., et al. 2011, in *General Assembly and Scientific Symposium, 2011 XXXth URSI, IEEE*, 1–4
- Leroy, A. K., Hughes, A., Schrubba, A., et al. 2016, *ApJ*, 831, 16
- Leroy, A. K., Usero, A., Schrubba, A., et al. 2017, *ApJ*, 835, 217
- Lique, F., Spielfiedel, A., & Cernicharo, J. 2006, *A&A*, 451, 1125
- Liszt, H. S., Lucas, R., & Pety, J. 2006, *A&A*, 448, 253
- Lombardi, M., Alves, J., & Lada, C. J. 2015, *A&A*, 576, L1
- Lucas, R., & Liszt, H. S. 2002, *A&A*, 384, 1054
- Mangum, J. G., Darling, J., Henkel, C., & Menten, K. M. 2013, *ApJ*, 766, 108
- Martín, S., Mauersberger, R., Martín-Pintado, J., Henkel, C., & García-Burillo, S. 2006, *ApJS*, 164, 450
- Martín-Doménech, R., Muñoz Caro, G. M., & Cruz-Díaz, G. A. 2016, *A&A*, 589, A107
- Matsushita, S., Kohno, K., Vila-Vilaro, B., Tosaki, T., & Kawabe, R. 1998, *ApJ*, 495, 267
- Matsushita, S., Muller, S., & Lim, J. 2007, *A&A*, 468, L49
- Mauersberger, R., & Henkel, C. 1989, *A&A*, 223, 79
- Meier, D. S., Walter, F., Bolatto, A. D., et al. 2015, *ApJ*, 801, 63
- Nishimura, Y., Watanabe, Y., Harada, N., et al. 2017, *ApJ*, 848, 17
- Padoan, P., & Nordlund, Å. 2002, *ApJ*, 576, 870
- Pety, J., Guzmán, V. V., Orkisz, J. H., et al. 2017, *A&A*, 599, A98
- Schinnerer, E., Weiß, A., Aalto, S., & Scoville, N. Z. 2010, *ApJ*, 719, 1588
- Schinnerer, E., Meidt, S. E., Pety, J., et al. 2013, *ApJ*, 779, 42
- Shirley, Y. L. 2015, *PASP*, 127, 299
- Soma, T., Sakai, N., Watanabe, Y., & Yamamoto, S. 2018, *ApJ*, 854, 116
- Tang, X. D., Henkel, C., Chen, C.-H. R., et al. 2017, *A&A*, 600, A16
- Usero, A., Leroy, A. K., Walter, F., et al. 2015, *AJ*, 150, 115
- van der Tak, F. F. S., Black, J. H., Schöier, F. L., Jansen, D. J., & van Dishoeck, E. F. 2007, *A&A*, 468, 627
- van der Tak, F. F. S., van Dishoeck, E. F., & Caselli, P. 2000, *A&A*, 361, 327
- van Dishoeck, E. F., Blake, G. A., Jansen, D. J., & Groesbeck, T. D. 1995, *ApJ*, 447, 760
- Vinkó, J., Takáts, K., Szalai, T., et al. 2012, *A&A*, 540, A93
- Watanabe, N., & Kouchi, A. 2002, *ApJL*, 571, L173
- Watanabe, Y., Nishimura, Y., Harada, N., et al. 2017, *ApJ*, 845, 116
- Watanabe, Y., Nishimura, Y., Sorai, K., et al. 2019, *ApJ*, in press (arXiv:1904.12430)
- Watanabe, Y., Sakai, N., Sorai, K., Ueda, J., & Yamamoto, S. 2016, *ApJ*, 819, 144
- Watanabe, Y., Sakai, N., Sorai, K., & Yamamoto, S. 2014, *ApJ*, 788, 4
- Wiesenfeld, L., & Faure, A. 2013, *MNRAS*, 432, 2573